IL NUOVO CIMENTO Vol. 24 C, N. 3 Maggio-Giugno 2001

Extreme Universe Space Observatory—EUSO: an innovative project for the detection of extreme energy cosmic rays and neutrinos

O. Catalano

Istituto di Fisica Cosmica con Applicazioni all'Informatica del CNR
Via Ugo La Malfa 153, 90146 Palermo, Italy

(ricevuto il 10 Gennaio 2001; approvato il 7 Febbraio 2001)

Summary. — The detection of extreme energy cosmic rays and neutrinos is the challenge of the future generation experiments in astroparticle physics. To extend our knowledge on the origin of the highest-energy cosmic rays and our understanding of particle interactions for $E > 10^{20}$ eV, we need the use of a detector with an effective area many times that of the today operative or planned experiments. The Extreme Universe Space Observatory—EUSO—meets this requirement and is the first experiment using the observation from a space-platform of the Earth atmosphere which behaves like an active detector for these extreme energy primary events. The air fluorescence of the extensive air showers produced by primary particles penetrating the Earth atmosphere is imaged by the EUSO telescope as the UV light progresses down through the atmosphere. A novel approach based on the single-photon counting and fast timing image technique permits to resolve arrival direction, energy and nature of the primary cosmic ray. The EUSO telescope conception, detection technique, system electronics and operating parameters are evaluated and discussed in this paper together with the planned mission profile and the operational performance expected.

PACS 96.40 – Cosmic rays.
PACS 13.85 – Hadron-induced high- and super-high-energy interactions (energy > 1 GeV).
PACS 95.30 – Fundamental aspects of astrophysics.
PACS 98.80 – Cosmology.

1. – Introduction

Particles with energy around and exceeding 10^{20} eV have been unambiguously identified in the primary cosmic-rays flux reaching Earth (see, *e.g.*, [1] and references therein); the Extreme Energy Cosmic Rays (EECR) and neutrinos with comparable energies represent one of the most intriguing phenomena of our physical world. The energy domain involved is only few decades below the Grand Unification Energy (10^{24}–10^{25} eV), although still rather far from the Plank mass of 10^{28} eV. The understanding of origin

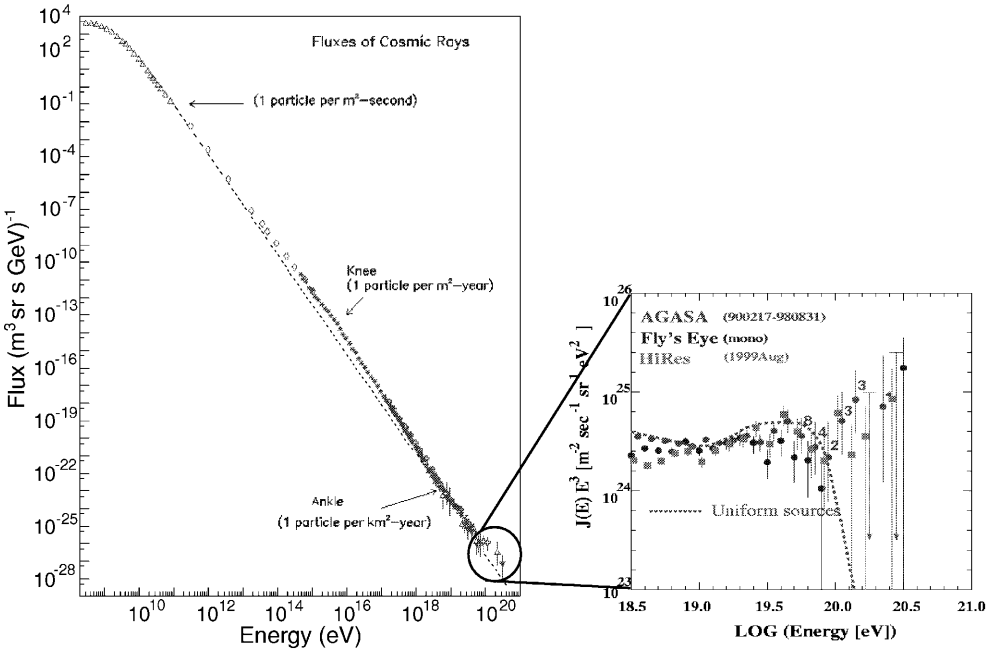

Fig. 1. – The observed cosmic-ray spectrum $> 10^8$ eV showing the principal features. The inset shows the high-energy part as observed by AGASA, Fly's Eye and HIRes. The dashed line shows the effect of the GZK cutoff assuming a homogeneous source population filling the Universe. The numbers shown for each point are the actual number of events in the bin.

and nature of these extreme energy events plays a role of major importance for astrophysics, cosmology and fundamental physics. The very low flux of EECRs is, on the other hand, a strong limiting factor for the comprehension of their role in the Universe. In fact, in spite of the big efforts lavished in the last 40 years, no more than a handful of events in this category has been reported by the ground-based experiments: one event from Volcano Ranch [2], four events from Haverah Park [3], one event from Fly's Eye [4], six events from Akeno [5], and seven events by Hi-Res preliminarily announced at the Metepec-Puebla Workshop, 2000. The scarcity of information, due to the small number of experimental data available, feeds the debate on the sources and propagation mechanisms of this radiation: proposed Bottom-Up [6] and Top-Down [7] processes are nowadays competing acceleration models. A point of discussion is represented by the change in the spectral index at $\sim 5 \times 10^{18}$ eV (the so-called "ankle"), as shown in fig. 1, which could correspond to a change in the primary elemental composition connected with a different source or confinement region in space, or to a change in production mechanism in the original sources, or even to a change in the interaction process leading to their detection at Earth. Another implication derives from the extension of the cosmic-ray energy spectrum observed above the Greisen-Zatsepin-Kuzmin limit (GZK $\sim 5 \times 10^{19}$ eV), connected with the energy loss mechanism of pion photo-production in the interaction of hadronic particles with the cosmic microwave background radiation at 2.7 Kelvin. This effect limits the distance of the sources of primary EECRs to less than 50–100 Mpc from our Galaxy, imposing a boundary to the possible astrophysical emitting sources. At present, no evidence of known astronomical objects has been reported associated with

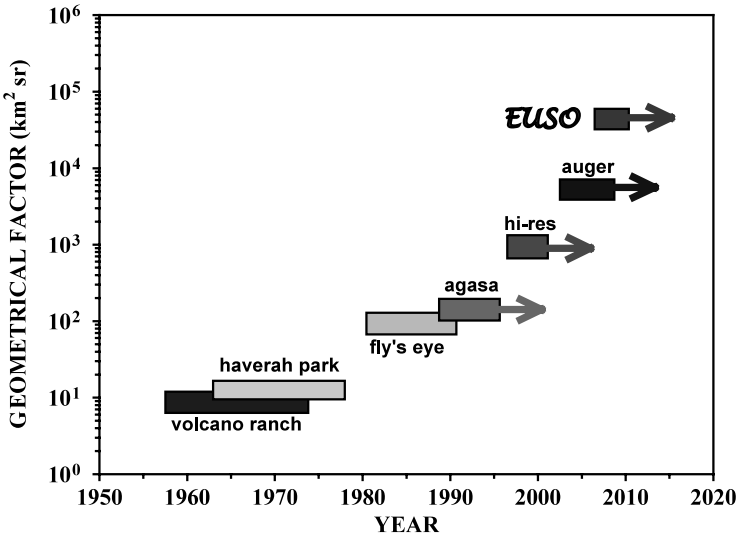

Fig. 2. – A comparison of the EUSO effective area with that of ground-based experiments, past, present and planned.

the arrival directions of cosmic rays above the GZK energy, leaving their origin an open question.

High-energy neutrinos could provide precious information about their origin together with that of the EECRs. Moreover, not suffering from the GZK effect and being immune from magnetic-field deflection and, if massless, from delay caused by the Lorentz factor, neutrinos are in fact ideal for tracking the sources and disentangling source related mechanisms from propagation related effects. On the other hand, the very weak interaction of the neutrino turns it in an elusive particle requiring a very massive target for its detection. The opening of a neutrino astronomy channel, not available for the experiments carried out up to now, will allow to probe the extreme boundaries of the Universe in the Gpc range. In order to explore this puzzling scenario, a substantial number of events of good quality is needed to improve the statistical significance of the overall data set.

The "Extreme Universe Space Observatory—EUSO", presently under assessment by the European Space Agency for accommodation on the International Space Station (ISS) in view of a mission starting in 2006-2007, has been designed to deal with this issue. The EUSO scientific payload is devoted, by observing the nocturnal part of the Earth from a space platform, to record the fluorescence signal generated by the Extensive Air Showers (EAS) initiated by the primary cosmic rays, including gammas and neutrinos. The main merit of this approach, suggested for the first time by John Linsley in 1979 [8], consists in providing a geometrical factor (km^2 sr) a step up of at least one order of magnitude compared to that of planned or already built ground-based experiments. The EUSO geometrical factor of $\sim 5 \times 10^5$ km^2 sr, shown in fig. 2, is obtained by using wide-angle optics with Field of View (FOV) of $\pm 30^\circ$ on board of a space platform at an orbit altitude of about 400 km: a duty cycle of 10% is assumed to take into account the interference introduced by the Sun and Moon, together with other UV background sources and the limitations connected with the cloud system. An important figure of merit for EUSO is the air target mass, exceeding 10^{12} tons, under its control. Mass and volume of the

target are suitable to catch the high-energy neutrinos, if the predictions reported in the literature on high-energy neutrino flux are realistic.

2. – The "observables"

The Earth atmosphere constitutes a natural absorber/converter detector for the cosmic radiation. High-energy cosmic-ray primaries (including gamma-rays and neutrinos) colliding with air nuclei produce secondaries that in turn collide again giving rise to a propagating cascade of particles. In the complex hadron-electromagnetic cascade represented by the EAS the most numerous particles are electrons. Electrons (and the other charged particles) moving through the atmosphere ionize the air molecules and excite metastable bound "electron levels" in the air atoms and molecules. With a short relaxation time, electrons from those levels return to the ground status emitting a characteristic fluorescence light. In air the fluorescence extends from the IR to the UV, with peaks at wavelengths from 330 nm to 450 nm (narrow lines at 337 nm; 357 nm; 391 nm). The photon yield in the atmosphere is about 4 photons/meter per relativistic electron track, roughly independent of the sea level altitude, due to the combined effect of density and re-combination processes [9]. The emitted light is isotropic and proportional to the shower size at any given depth in the atmosphere. The number of electrons at shower maximum development $Ne_{\max}$, *e.g.*, is proportional to the energy of the primary particle E_{p} (eV) through $E_{\mathrm{p}} = E_{\mathrm{m}} \times Ne_{\max}$, where $E_{\mathrm{m}} \sim 1.3 \times 10^9$ eV. The signal resulting from the "fluorescence" process, when the UV photons are collected from some detection points, provides therefore a measure of the energy of the primary particle. This method is referred to as "calorimetric" with a direct allusion to the energy deposited by the charged particles belonging to the EAS in the atmosphere.

A high-energy EAS forms a significant streak of scintillation light along its passage in the atmosphere: observation of this emission with a detector at distance from the shower axis is the best way to control the cascade profile. The shower appears as a relatively small disc-shaped luminous object emitting isotropic light; when viewed continuously, the object moves on a straight path with velocity c identifying the arrival direction of the primary. As it does so, the disc luminosity changes from so faint to be undetectable up to a maximum followed by a gradual fading. The resulting time-integrated image seen by the detector looks like a narrow track in which the recorded amount of light is proportional to the shower size (electron content) at the various penetration depth in the atmosphere. From the integral of light recorded in the track (as well as the light signal at shower maximum) we derive the primary energy. The cascade shape (especially the position of the shower maximum as a function of the penetration depth) gives an indication about the nature of the primary. A different shape for the cascade curve is expected for different particles initiating the EAS: while hadron- or gamma-initiated showers start in the upper layers of the atmosphere ($\lambda \sim 50$–70 g/cm^2), showers initiated very deep indicate an origin by neutrinos, the neutrino-air nuclei interaction cross-section being several orders of magnitude lower than the cross-section for hadrons or photons as shown by the simulation of fig. 3 where $X_{\max}$ indicates the height (g/cm^2) at which the EAS presents its maximum development.

The fluorescence method has been successfully implemented on ground-based experiments by Fly's Eye [10] in the past and presently by HiRes [11] in Utah; it is planned, in combination with an array of Water Čerenkov particle detectors, as baseline for the Auger project [12]. From a Low Earth Orbit (LEO) space platform, free-flyer or anchored to the Space Station, the UV fluorescence induced in the atmospheric nitrogen by the

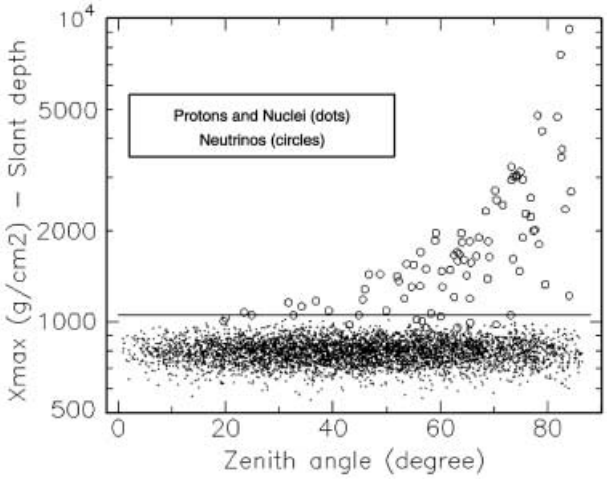

Fig. 3. – Downward-going neutrino events penetrate deep into the atmosphere before starting an EAS. They can be discriminated from protons (and photons) with very high efficiency by a selection criterion on the depth of the starting point of the shower (deeper than 10^3 g/cm^2 for the "Neutrino region"). The figure shows Monte Carlo simulation of shower maximum ($X_{\max}$) distributions for protons and neutrinos, respectively.

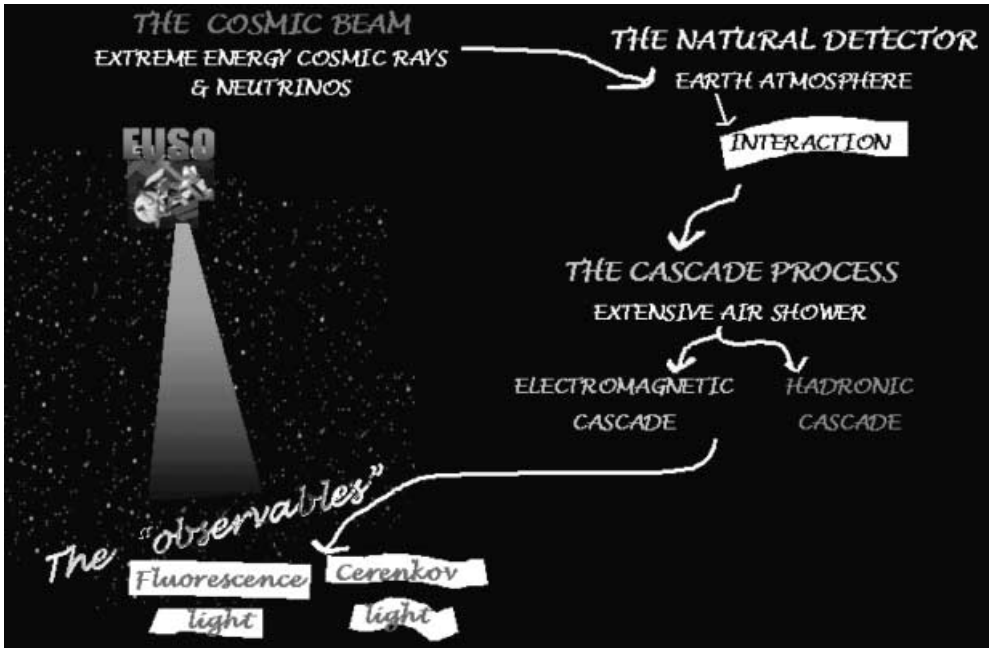

Fig. 4. – Sketch of road-map of the process leading to the "observables".

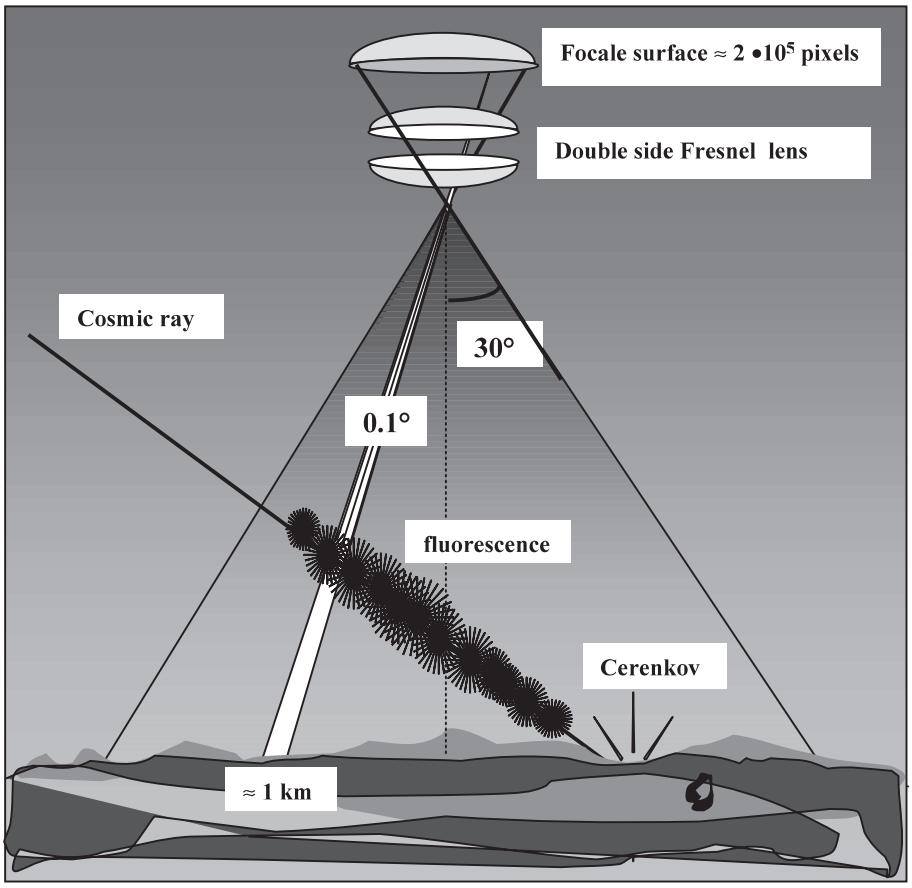

Fig. 5. – Scheme of an EAS track and the characteristic UV emission associated.

incoming radiation can be monitored and studied; the luminescence coming from EAS produced by the cosmic-ray quanta (protons, nuclei, gamma-rays, neutrinos,...) can be disentangled from the general background and measured. A road-map of the process leading to the "observables" is sketched in fig. 4. Other phenomena such as meteors, lightning, atmospheric flashes, distribution of minor components in the atmosphere, can also be observed.

3. – The EUSO approach

The relativistic shower of particles generated by a cosmic-ray primary with energy above 10^{19} eV penetrates the Earth's atmosphere for a length as long as 10–100 km (or longer) depending on the angle of incidence to the vertical; the duration of this passage correspondingly lasts for 30–300 μs. Figure 5 illustrates schematically an extensive air shower track and the characteristic UV emission associated.

The atmospheric fluorescence light provides the main signal to reconstruct the longitudinal development of the EAS, while the flash of isotropic light produced by the impact of the Čerenkov beam hitting ground or the cloud top provides the identification of the

thickness of the layer of atmosphere involved and the scale height. The number of fluorescence photons (proportional to the number N_e of charged particles present in the EAS front) sampled at constant intervals of time is converted by the telescope in a number of photoelectrons with dependence on atmospheric transmissivity, collection efficiency of the optics and quantum efficiency of the detectors in the focal surface. The conversion from N_{pe} to N_e is obtained deconvolving the telescope data into the input signal by using the "response matrix" of the instrument; finally the primary particle energy is deduced by adopting a "correspondence relation" given by a simulation procedure based on an elaborated Monte Carlo computation of the chain of processes involved in the cascade giving rise to the EAS. An average value for the nightglow background is assumed, by using the data from satellite [13] and balloon-flight [14] measurements in the relevant wavelength range ($\sim$ 200 photons m^{-2} sr^{-1} ns^{-1} in moonless condition). The sequence of the shower development along the vertical depth of air can be analyzed by the spatial and temporal transition of the fluorescence intensity, as well as by using the landmark reflected Čerenkov signal (fig. 5).

The tracing of a primary particle back to the astrophysical source requires an adequate angular resolution: for charged primaries the presence of magnetic fields along the trajectory introduces, on the other hand, a substantial bending. The EUSO technique allows the identification of the shower axis direction with a good resolution using the spatial information of the imaged track combined with the fast timing information. This is obtained by combining the azimuth angles of the EAS track projected in the plane perpendicular to the line of sight with the zenith angle resulting by considering the velocity of progression of the projected track (see subsubsect. **4**˙3.2). Monte Carlo simulations of atmospheric fluorescence signals of ordinary downward events show that the angular resolution for EUSO varies from 0.2° to 3°, depending on the primary energy and particle zenith angle. Better values for the angular resolution can be obtained if is used the Čerenkov landmark reflected signal as a prolongation of the shower axis up to the impact of it on ground, clouds or sea. Figure 6 compares qualitatively the expected error box on the pointing directions for neutrino and proton respectively for an average source distance of 30 Mpc and an average intergalactic magnetic field of 1 nGauss.

4. – The EUSO telescope

The mission EUSO has been proposed to the European Space Agency in January 2000 in response to the Announcement of Opportunity for the F2/F3 program issued in October 1999. The proposal, originally intended for a Free Flyer Satellite in equatorial circular orbit at 500 km height, has been selected in March 2000 for an accommodation study as external payload for the ISS.

The monocular stand-alone configuration of the telescope is capable to detect EECRs and neutrinos events at energies higher than $\sim 4 \times 10^{19}$ eV, looking downward the night side of the Earth, from the distance of about 400 km, averaged orbit altitude of the ISS. The capability to detect fluorescence events using the monocular approach is of fundamental importance for a space-based experiment to meet the stringent requirements for power consumption, weight, volume and cost.

The EUSO telescope design has been conceived as a compact instrument, as schematized in fig. 7. The monocular instrument configuration is the result of a close synergy in the design of the optics, focal surface detector and the system electronics governing the entire system. New and innovative ideas have been introduced. Optics of very wide field of view and large collecting area has been designed, using Fresnel lens technology,

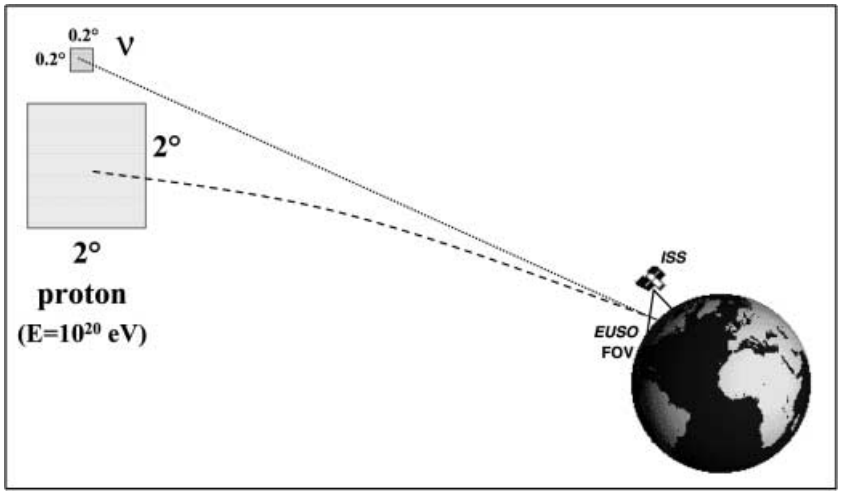

Fig. 6. – Qualitative comparison of the expected error box on the arrival direction for neutrino- and proton-induced EAS.

to achieve the requirement of a low focal number, full aperture of 60° and lens diameter of 2.5 meters (entrance pupil equal to 2 meters). The UV sensors for observing the images corresponding to the EAS tracks have been selected taking into account the requirements imposed by the project: in particular concerning the pixel size, the gain, the fast response time and the low weight and dimension. To detect the very faint fluo-

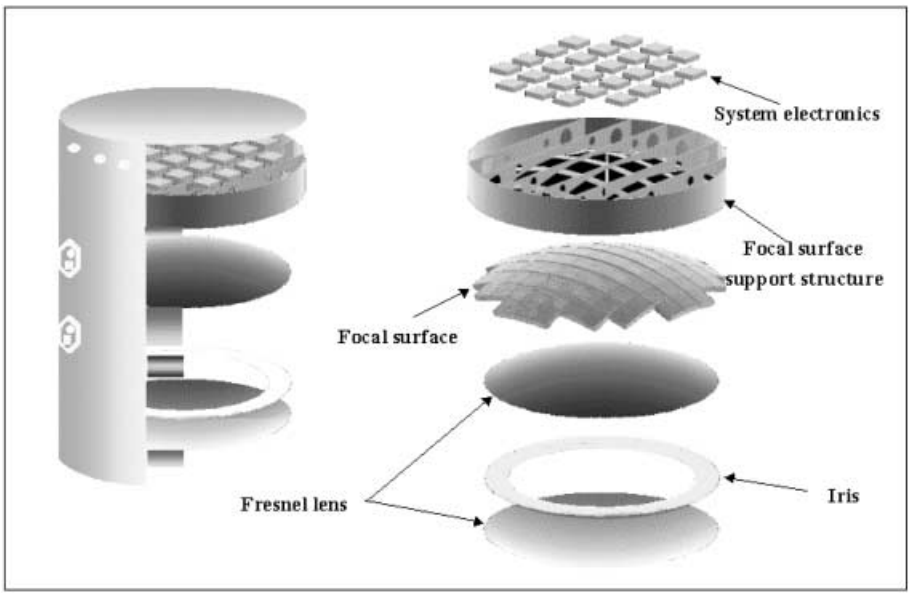

Fig. 7. – Overall scheme of the EUSO telescope: cross-section (left) and exploded view (right) of the telescope.

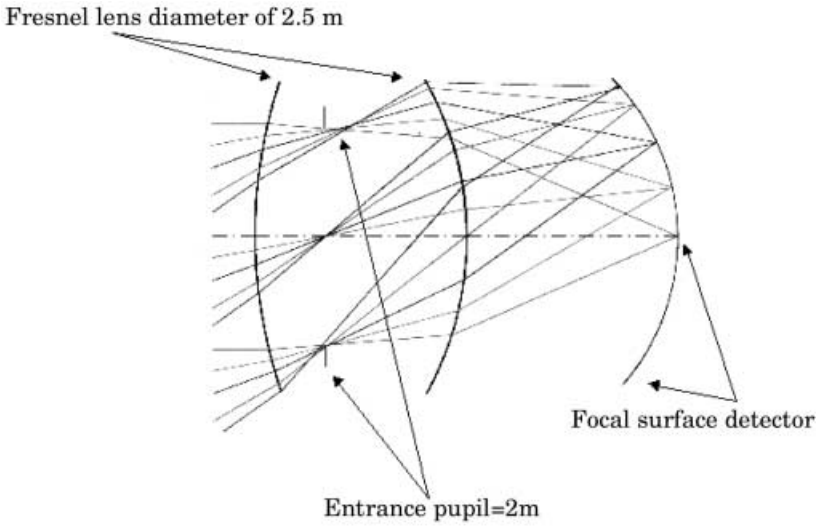

Fig. 8. – The double Fresnel configuration adopted for EUSO.

rescence signals on the relatively intense background level, a novel method, based on the single photon-counting and fast timing technique, has been adopted to design the EUSO System electronics. A description of the elements constituting the telescope is given in the following, with details of the system electronics responsible for the data read-out, data handling and triggers.

4˙1. *The optical system.* – EUSO imaging requirements are rather forgiving: a moderate angular resolution of 6 arcmin (10^4 times more than the diffraction limit) is sufficient to image the streak produced by a EAS in the atmosphere. At the height of 400 km the space resolution requested at ground is about 0.8 km, few times the "Molier" radius that accounts for the lateral growth of the cosmic-ray shower because of the multiple Coulomb scattering of the electrons in their final path. A more stringent demand is required for the angle of aperture with a total field of view of 60 degrees.

The large dimension of the optics imposes lightweight materials with mechanical properties suitable to resist the launch environment conditions (*i.e.* a high specific Young modulus, dimension stability, high limit of elasticity, etc.) and vacuum environment; the operating conditions in orbit require moreover the adoption of Radiation Hard technology. Polymer materials with the required characteristic and UV transmittance of the order of 90% in the 330–430 nm band have been identified and selected.

Figure 8 shows the double Fresnel configuration adopted for EUSO.

To limit the dimension of the focal surface, a focal number $f/\#$ close to 1 has been chosen ($f/\#$ = focal length/entrance pupil diameter). The etendue principle establishes that

$$n_{\mathrm{pe}}^2 \cdot A_{\mathrm{pe}} \cdot \Omega_{\mathrm{pe}} \;=\; n_{\mathrm{d}}^2 \cdot A_{\mathrm{d}} \cdot \Omega_{\mathrm{d}}\,, \tag{1}$$

where A_{pe} is the pupil entrance area, Ω_{pe} the entrance pupil solid angle, A_{d} the detector area, Ω_{d} the detector solid angle, and n_{pe} and n_{d} the refraction index of the medium containing entrance pupil and detector, respectively. Calling α the half-angle of the

light cone subtended by the pupil entrance (FOV) and β the half-angle of the light cone of maximum inclination reaching the detector (marginal rays), the expression for the etendue invariant in eq. (1), assuming the system is lossless, can be written as

$$n_{\mathrm{pe}}^2 \cdot A_{\mathrm{pe}} \cdot 2 \cdot \pi \cdot (1 - \cos\alpha) \;=\; n_{\mathrm{d}}^2 \cdot A_{\mathrm{d}} \cdot 2 \cdot \pi \cdot (1 - \cos\beta)\,. \tag{2}$$

From this expression some geometrical quantities can be determined; in particular the focal surface size is given by

$$A_{\mathrm{d}} \;=\; (n_{\mathrm{pe}}/n_{\mathrm{d}})^2 \cdot A_{\mathrm{pe}} \cdot (\sin^2(\alpha/2)/(\sin^2(\beta/2))\,. \tag{3}$$

Considering equal to unity the indices of refraction (for optical system operated in vacuum) and using for the angle β the geometrical relation $\beta = \arctan(1/(2 \cdot f/\#))$, eq. (3) can be rewritten as

$$A_{\mathrm{d}} \;=\; A_{\mathrm{pe}} \cdot \sin^2(\alpha/2)/\sin^2(1/2 \cdot \arctan(1/(2 \cdot f/\#)))\,. \tag{4}$$

The pixel size corresponding to the spot size diameter d_{spot}, that measures the resolution of an optical system, is determined by the effective focal length (EFL) and the resolution required by the optical system. For EUSO the required resolution θ is of the order of 0.12° corresponding to the on-ground selected resolution (0.8 km); this yields the pixel diameter at about 5 mm as indicated by

$$d_{\mathrm{spot}} \;=\; EFL \cdot \tan\theta\,. \tag{5}$$

The EUSO optical system requires a bandpass filter (330–430 nm) to prevent light of undesirable wavelength from reaching the focal surface. Candidate elements are commercial BG1 or BG3 absorption filters [15]. Interference filters are also considered for their suitability to be deposited on the lens surface.

Iris mechanism to prevent the focal surface detector from the reflected/diffused light during the diurnal orbit phase has been introduced in the optics system. The iris protects also the telescope from the environmental pollution produced during the scheduled periodic Shuttle docking.

Figure 9 shows a reduced scale prototype unit built at the Optics Center of the University of Alabama in Huntsville.

4˙2. *The focal surface detector.* – The optical system must be closely integrated with the focal surface detector. This imposes a specific and appropriate design so that the image quality is not compromised. A "tiled" focal surface has been preferred for adapting the detector units to a curved surface, resulting from the adoption of Fresnel optics configuration. The focal surface is constituted by about hundreds tiles, called "macrocells". A macrocell is formed by 6×6 MAPMTs (multi-anode photomultipliers). The MAPMT photocatode, manufactured by Hamamatsu (series R7600-M64 [16]), is organised in an array of 8×8 pixels. Figure 10 shows the hierarchical organisation of the focal surface detector.

This commercial multi-anode photomultiplier in the version currently available has characteristic close to the requirements concerning the pixel size, the gain, the fast response time and the low weight (30 grams) and dimension ($25.7 \times 25.7 \times 33$ mm^3).

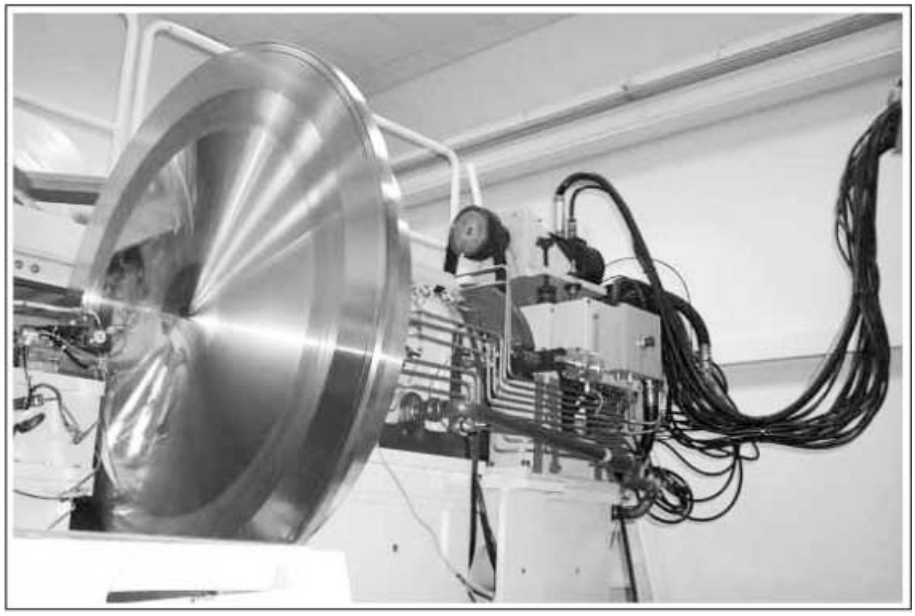

Fig. 9. – A reduced scale prototype unit built at the Optics Center of the University of Alabama in Huntsville.

This MAMPT also exhibits a very low cross-talk of the order of 2% and a good response uniformity characteristic. The phototube is equipped with a bialkali photocatode and an UV transmitting window that assure an average quantum efficiency of the order of 20% in the wavelength range of 330–430 nm. The gain provided by this device at the nominal working parameters (3×10^5 at 900 V) avoids the use of fast, low-noise and consequently high-power consuming preamplifiers, simplifying the front-end design and reducing drastically the power required. The pixel size of the R7600-M64 is 2 mm with the pixels organised in a central matrix of 8×8 pixels leaving a dead external area covering about 50% of the total physical dimension of the entrance window of the photomultiplier. To overcome this limitation, a suitable light collector system needs to be placed in front of each phototube to perform the demagnification required to assure the matching between the continuous focal surface image and the geometry of the MAMPTs; this leads to consider the dimension of the pixel as the one resulting from the demagnification light collector system. Figure 11 shows a demagnification system based on a bundle of tapered reflective light pipes. Other systems such as refractive tapered light pipes or plane-convex hemispherical lens could be used for re-focus the incident rays on the active surface.

Special consideration must be given to the power consumption required to operate the MAPMT. Average anode current is determined considering the average background light received by a pixel in the EUSO configuration. With an assumed night light background level $\langle B_{\mathrm{bkd}} \rangle$ of the order of 200 photons $\mathrm{m}^{-2}\ \mathrm{sr}^{-1}\ \mathrm{ns}^{-1}$, an overall efficiency ϵ_{tot} (optics transmission, filter transmission, light guide, detector Q.E.) of 0.12, and a lens collecting area (entrance pupil) A_{lens} of 2 meters, the average photoelectrons (pe) number per pixel

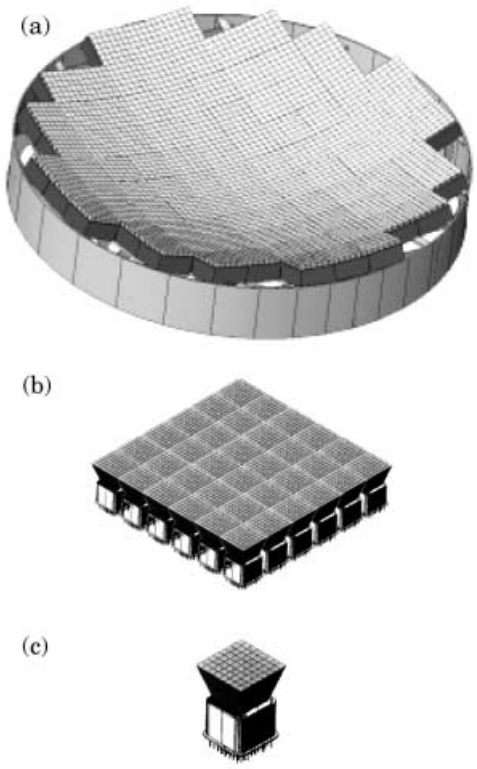

Fig. 10. – (a) A schematic of the EUSO focal surface assembly showing how the individual macrocells are mounted to approximate the curve focal surface of the optics. (b) Each macrocell consists of 6×6 Photomuliplier Tube assemblies, associated light guides and electronics and is a modular unit. (c) Each PMT is a commercially available 8×8 multi-anode device; here it is shown with a possible light guide used to match the active area to the focal surface.

(in a time unit TU of 800 m/c, with c speed of light)

$$N_{\mathrm{pe}} \;=\; \langle B_{\mathrm{bkd}} \rangle \cdot \Omega_{\mathrm{pixel}} \cdot A_{\mathrm{lens}} \cdot TU \cdot \epsilon_{\mathrm{tot}} \tag{6}$$

amounts to 0.7 that turns out to be about 45 pe for a 8×8 pixels MAPMT unit. The background rate per photomultiplier will be then of the order of 20 MHz. The average background anodic current per tube can be written as

$$\langle I_{\mathrm{bkd}} \rangle \;=\; 64 \cdot (N_{\mathrm{pe}}/TU) \cdot G \cdot e\,, \tag{7}$$

where G is the tube gain and e is the electron charge. Substituting the numerical values in eq. (7), an average background anodic current of the order of 1 μA is obtained. The average current due to the single pe is

$$\langle I_{\mathrm{pe}} \rangle \;=\; 2 \cdot G \cdot e/t_{\mathrm{pulse}} \tag{8}$$

with $t_{\mathrm{pulse}} = 3$ ns representing the width of the output pulse. The average single pe current results about 30 μA. It is easy now to calculate the peak average current for a limit

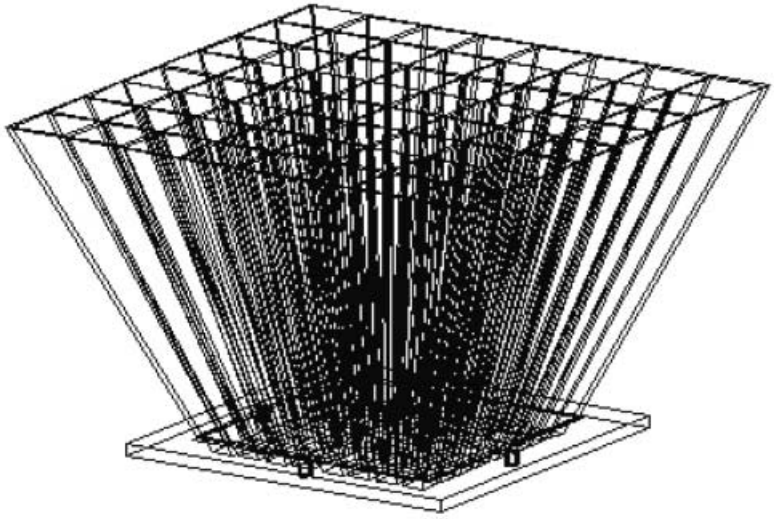

Fig. 11. – A demagnification system based on a bundle of tapered reflective light pipes.

event of energy 10^{21} eV. Assuming a total number $N_{\rm pe} \sim 30000$ in a time $T = 330$ μs, the peak current will be

$$\langle I_{\rm peak} \rangle \;=\; \langle I_{\rm pe} \rangle \cdot N_{\rm pe} \cdot t_{\rm pulse}/T \tag{9}$$

giving a peak event current of the order of 10 μA. From the considerations above, a suitable low-power voltage divider, not affecting the output linearity, can be designed and optimized in a way to reduce the power consumption of the entire focal surface detector at less than 100 Watts.

4˙3. *The system electronics.* – Signal-to-noise ratio optimization, "image" segmentation and "free running" method are the main constituents of the system electronics designed for EUSO [17].

Faint signal detection is normally achieved using single-photon counting technique. Information from the physical phenomena is usually carried by coherent signals against incoherent environmental background. The background measured by any sensors (UV in our case, with an order of few nanoseconds resolving time) competes generally with signals from sources or features that, although coherent in time and space, have comparable small intensity. A method devoted to enhance the signal-to-noise ratio has been developed; its hardware implementation, the "Pixel Front-End" (PFE) is part of the System Electronics design.

Modularity of the "image" space, provided by the focal surface detector and electronics associated, satisfies not only the requirements of flexibility, easy planning and implementation but also, in case of space experiments, represents a fundamental parameter contributing to a space mission success. Independent stand-alone macrocell operations and reduction of the total number of read-out channels are other important aspects of the design. The characteristics of the design of the macrocells and associated read-out are part of the FIRE (Fluorescence Image Read-out Electronics) system.

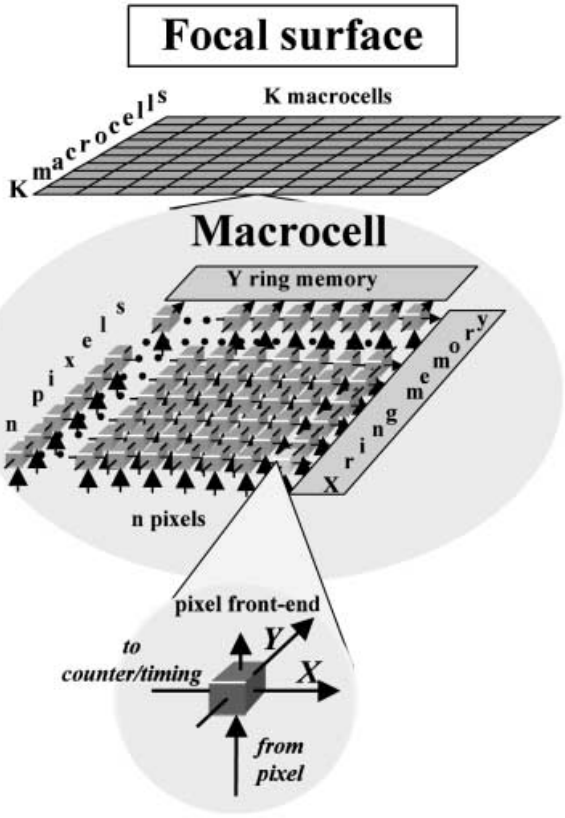

Fig. 12. – The EUSO detection system: hierarchical organization from the pixel front-end to the focal surface.

The "free running" method adopted is based on the continuously writing of the information into macrocell ring memories until a stop signal, derived from a specialized trigger unit, stops the writing operation. At the stop signal a reading operation is started that enables accessing the information recorded in the memories. The "free running" method is an integrating part of the trigger and control module OUST (On-board Unit System Trigger) and it plays a basic role in the EUSO System Electronics.

Figure 12 shows the hierarchical organization of the EUSO detection system, whereas in fig. 13 the block diagram of the EUSO System Electronics is shown.

4˙3.1. PFE. The Pixel Front-End is the electronics section interfacing the detectors to the read-out electronics. The most significant feature concerning this front-end electronics design is the capability to enhance the signal-to-noise ratio using the Poissonian statistics property applied to the specific phenomena considered.

The Poissonian probability to find in one pixel at least n photoelectrons in one time unit TU is

$$P_{N_{\rm pe}}(\geq n) \;=\; 1 - \sum_{m=0}^{n} \frac{N_{\rm pe}^{m}}{m!} e^{-N_{\rm pe}}\,, \tag{10}$$

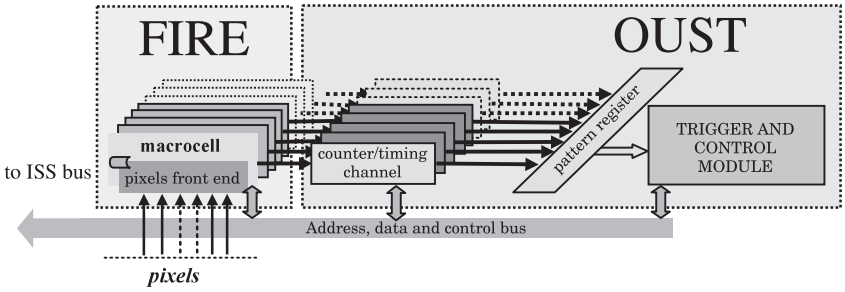

Fig. 13. – The EUSO System Electronics: block diagram.

where $N_{\rm pe}$ is given by eq. (6). The resulting Signal-to-Noise Ratio SNR then is

$$SNR = \frac{S - n + 1}{\sqrt{P_{N_{\rm pe}}(\geq n)}}, \tag{11}$$

where S is the signal per pixel per time unit TU and $P_{N_{\rm pe}}$ is given by eq. (10).

Using a digital counter and an AND-gate it is possible to implement this function as shown in fig. 14. Following the block diagram in the figure, photo-electron analog pulses are discriminated and shaped by a fast threshold discriminator. The formed digital outputs are sent to the clock input of the digital counter. Setting the "set counter" input of the programmable counter at an integer value n makes the Q output "true" when the counter reaches the value n, opening the AND-gate at the passage of the incoming digitized pulses that can now reach the macrocell counter/timing channel. The latched value at the Q output of the counter is routed to the X and Y Wired-OR connection lines. Using the above-defined EUSO parameters, the expected background, in case of a probability to find at least 1, 2, 3, or 4 photo-electrons in a pixel per time unit, is respectively shown in fig. 15 for a matrix of 240×240 pixels.

4˙3.2. FIRE. Figure 16 shows the macrocell organization. Each macrocell operates independently of the others macrocells: no inter-connection is present in the design. This characteristic permits to simplify the read-out scheme and in the same time to reproduce it in a modular way.

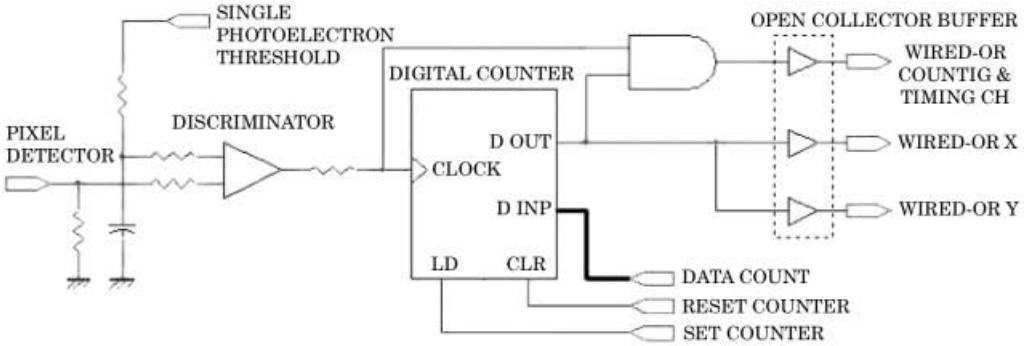

Fig. 14. – Electrical scheme of the PFE electronics.

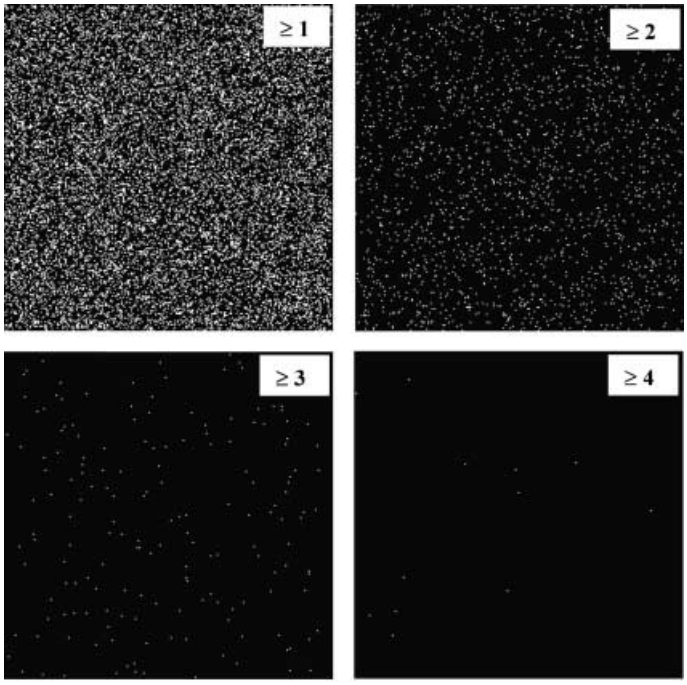

Fig. 15. – Expected background in a matrix of 240 × 240 pixels. White dots represent the distribution of pixels fired by imposing the probability of finding respectively at least 1, 2, 3, or 4 photoelectrons in a pixel per time unit.

Projected positions, number and arrival time (if required) x_i, y_i, N_i, t_i of the detected photoelectrons are recorded separately, every time unit, in the ring memory X and Y (outputs from the X and Y PFE Wired-Or) and in the counter/timing ring memory line (outputs from the counter/timing Wired-Or of the PFE). The ring memories have the capacity of holding the information for a time comparable at the longest physical event expected. Nowadays low consuming and large depth memories are available commercially (a memory of 256 kbytes can hold as much as more than 150 ms of information assuming a

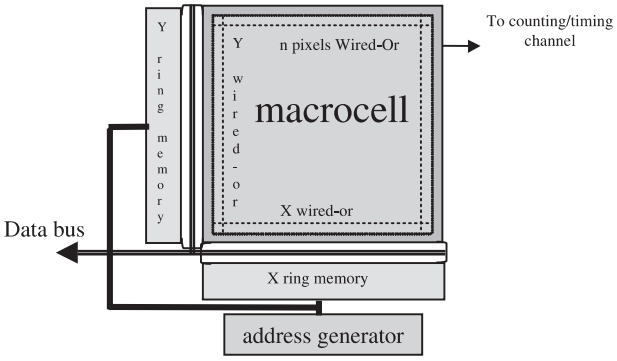

Fig. 16. – The macrocell organisation.

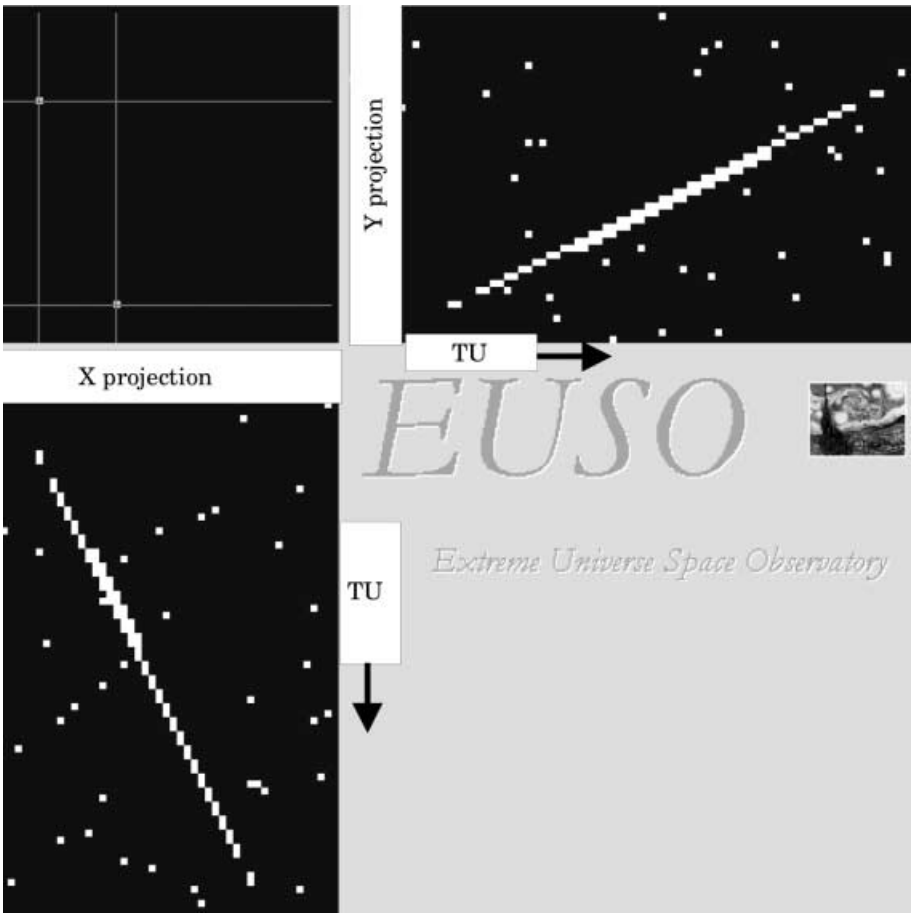

Fig. 17. – Representation of a typical track as stored in X and Y ring memories; sparse dots indicate the residual background.

time unit of 666 ns). Information containing the status of the rows and columns is written in binary format sequentially every time unit. In the absence of a trigger signal the ring memory will be continuously written updating the information stored. At a trigger signal the writing operation stops and the memory is read backward for an appropriate length given by a time unit counter. The addressing to the ring memory is controlled by a logic circuit that drives the address bus of the memory for the writing and reading operations. A representation of a typical track is shown graphically in fig. 17. Each line of the X and Y projection planes represents the contents of the related ring memory bytes per time unit resulting by Wired-Oring the rows and columns of the macrocell. In this representation the continuous lines are formed by reading respectively X and Y consecutive memory locations.

Arrival direction of the events is derived from the slopes of the linear tracks along the two projections, taking into account the kinematics of the relativistic particle,

$$\phi \;=\; \arctan\left(\frac{\Delta y}{\Delta x}\right) \qquad \theta \;=\; 2\cdot\arctan(C\cdot\sqrt{(\Delta x)^2+(\Delta y)^2})\,, \tag{12}$$

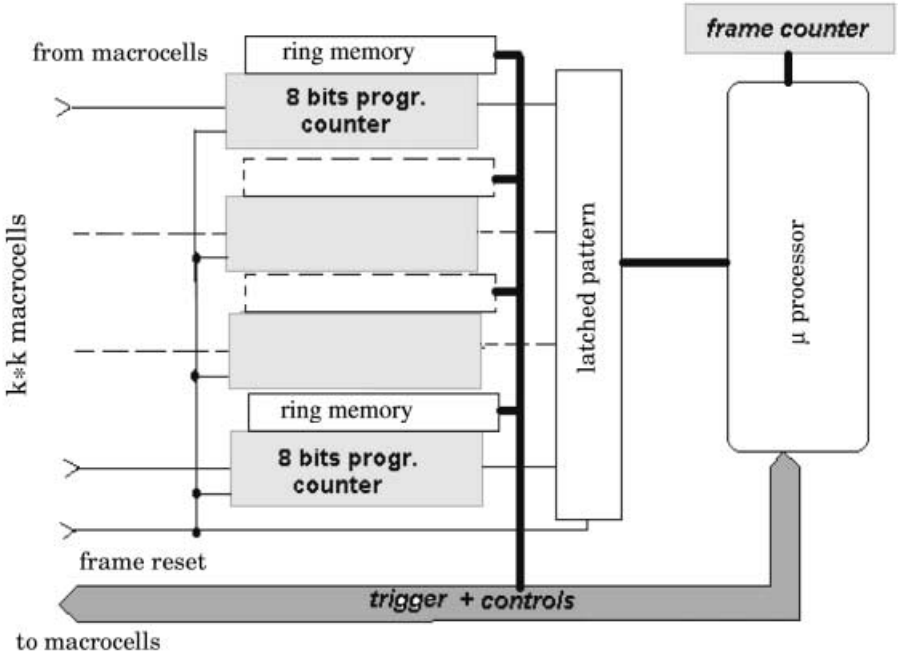

Fig. 18. – Architecture of the OUST system.

where ΔX and ΔY are the slopes of the projected track and C is a constant related to the speed of light and depending on the on-ground pixel size and on the time unit ($C = \Delta L/(c \cdot TU)$). The total number of photoelectrons (signal) per time unit can be calculated as

$$N_{\mathrm{pe}} \;=\; N_{\mathrm{pulses}} - N_{\mathrm{pixels}} + n\,, \tag{13}$$

where n is the integer number that sets the "set-counter" input of the PFE digital counter, N_{pulses} is the total number of pulses in a macrocell per TU, and N_{pixels} is the total number of projected pixels in a macrocell per TU.

4˙3.3. OUST. The On-board Unit System Trigger must be capable to trigger "events" deciding when "event data" are present without the intervention of any external condition. The block diagram of fig. 18 shows the OUST architecture. The signals (in form of digital pulses), coming from the counter/timing output of each macrocell, are sent to the OUST 8 bits programmable counters (one per macrocell). At every time unit the counters contents, *i.e.* the total number of photoelectrons over the "set-counter" binary threshold of the PFE digital counters belonging to each macrocell, are recorded into the OUST ring memories (one per macrocell) and then reset. The counters status reflecting a condition over an imposed "count" programmable threshold is passed, as one bit information, to a pattern register (with length equal to the macrocells number) and read-out at each time unit by a microprocessor.

An algorithm analyzes the persistence in time of the over-threshold (at level of 3 sigma for example) macrocell signals and enables a time unit counter if a persistence of a few time units is found in the same macrocell. If after this alert condition the macrocell

fails (no more persistence signal is found in the macrocell below a certain inferior limit given by the minimum duration of a shower track) the time unit counter is reset and the algorithm continues to seek. In case of an alert condition and persistence in time between the minimum and the maximum duration of a shower track, the microprocessor will send a signal to stop all the writing operation in the ring memories. The ring memories are read-out backwards for the appropriate length by using the "persistence count" information kept in the Time Unit counter. For persistence counting greater than the maximum allowable shower track duration, a second level of trigger is activated. Basically it will follow the same procedures as the first level trigger and it will be devoted to trigger slower atmospheric phenomena as meteoroids, blue jets, etc. Using eq. (10) multiplied by the number of pixels of a macrocell and substituting the value obtained in eq. (11) it is possible to optimise the signal-to-noise figure.

5. – The passive atmosphere: signal absorption, scattering, reflection

The geometry resulting by looking downward to the Earth atmosphere from the ISS, is simple and immediate and it reflects on the events observation procedures. The air fluorescence light produced isotropically by the EAS is attenuated by the absorption and scattering before arriving at a distant observer. The absorption, at the wavelengths of interest, *i.e.* $330 \leq \lambda \leq 430$ nm, is not significant in the ozone neither in water nor in CO_2 absorption wavelength range. Scattering is, indeed, the dominant effect at these wavelengths. Aerosol (Mie scattering) and air molecules themselves (Rayleigh scattering) are responsible for the major loss mechanisms for the propagation of light in the atmosphere. Mie scattering is a complex function of particles size and shape, refractive index, scattering angle and wavelength; it tends to be most important for small scattering angle and it is not a severe effect for EUSO because much of the light-path is above the aerosol zone which tends to be concentrated at low altitudes near ground. Rayleigh scattering is proportional to λ^{-4} and thus becomes the dominant effect for the shorter end of our wavelength range. Rayleigh scattering has a $1 + \cos^2\theta$ angular dependence, it is therefore important for all scattering angles.

The plot in fig. 19 shows the UV light transmission efficiency as a function of the wavelength as calculated for the ozone layer and Rayleigh scattering.

The air fluorescence light undergoes also diffusion/reflection and, to a some extent, scattering by clouds. Clouds play a two-fold role for the events observation. On the one hand, reflection on clouds of the Čerenkov and fluorescence light belonging to the EAS, is more efficient than on sea or ground, and it can be used as an independent estimator of the primary energy: on the other hand, part of the light (associated to the shower axis) could be hidden or diffused by the clouds if the clouds are very high in the sky (> 5 km) and contemporarily the shower has a small inclination. These effects, affecting the performance of EUSO, will be treated in a quantitative way in the next paragraph.

Atmosphere sounding by an on-board laser or equivalent system becomes important for the reasons above mentioned. At the information about the global property of the atmosphere in the zone of interest of the event (humidity, visibility, temperature, clouds) deduced by using data from the weather satellites network operating around the Earth, complementary "space-time" local information is represented by the use of an on-board LIDAR system. Shooting a laser beam after a triggered event is occurred, and by making a scanning in the direction around the landing point of the shower axis, provides the information needed about the overall atmosphere transmission efficiency and cloud altitude distribution.

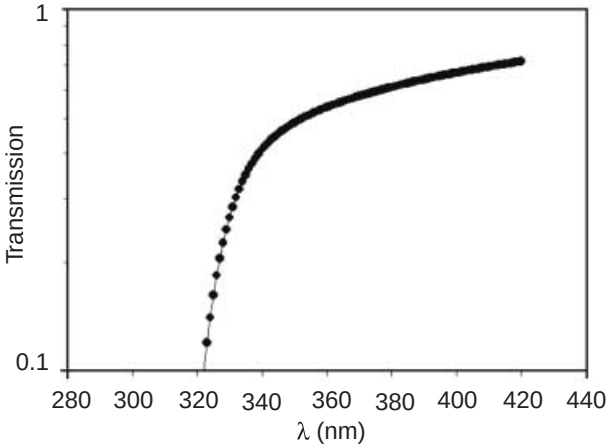

Fig. 19. – The UV light transmission efficiency as a function of the wavelength: the combined effect of atmospheric ozone layer and Rayleigh scattering has been evaluated for an air density column of 1200 g/cm^2.

6. – EUSO **Mission profile**

Following the recommendations of ESA as a result of the F2/F3 Announcement of Opportunities proposal selection on March 2000, EUSO has undergone during the year 2000 an "Accommodation Study" to assess the conditions for a mission on board of the International Space Station. The study foresees the accommodation of EUSO on the ESA-Columbus exposed payload facility.

An artistic view of EUSO accommodation on the ISS is shown in fig. 20.

EUSO is essentially a fixed nadir pointing observatory, and no specific observation plan is required. This configuration, with no possibility of rotational or translational movements, obviously simplifies the entire mission management in comparison with a pointing free-flyer satellite. A nominal three-years operation is foreseen for observations and data taking instead of the two years initially planned for the Free-Flyer configuration in order to compensate for the dead-time intervals in the duty cycle, connected with the operation procedures required by the ISS manouvres.

6˙1. *Performance*. – The response of EUSO, on board of the ISS, has been evaluated with an appropriate simulation software. The simulation of the physics aspects involved in the processes has been developed and used to feed the entire system including the System Electronics. The program (hereafter named "AWsim") [18] calculates the geometrical acceptance, trigger aperture and rates as a function of the primary energy. AWsim also generates detailed signals and timing information for all possible event geometry involved. It includes the geometrical constraints (pixel size, solid angle, acceptance) and the physics parameters (shower energy, fluorescence yield, clouds coverage, ...) which affect the measurement of an event. The curvature of the Earth as well as a standard model of the atmosphere which takes into account the response variation with temperature and altitude have been introduced in the program. The estimate of the EUSO event rate has been carried out testing and optimizing the output response to different triggering schemes.

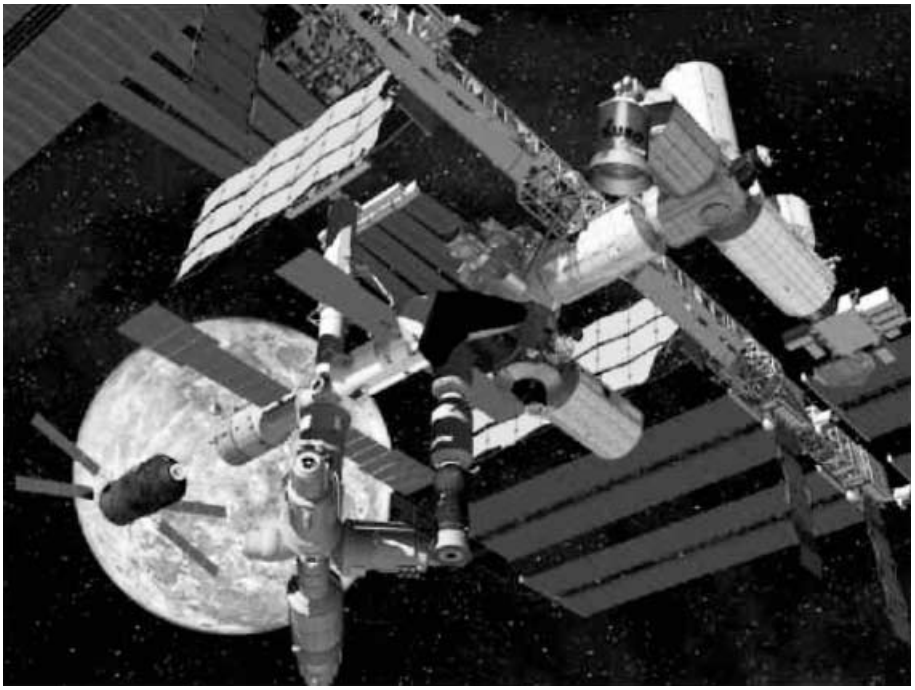

Fig. 20. – EUSO accommodated on the ISS: artistic view with Moon in the backdrop.

The longitudinal development of the shower is calculated by using the GIL (Greisen-I'ilina-Linsley) parameterization formula [19]. The GIL parameterization calculates the number of electrons N_{e} at different observational depth levels of the shower as a function of the primary energy. Showers are generated isotropically with the random parameters θ, ϕ, α, β (as defined in ref. [18]) and propagated into the atmosphere in steps of $\Delta L =$ 200 meters. The 200 m step (transformed coherently in g/cm^2) accounts for the time unit adopted (TU = 666 ns). For any of those steps, the x, y positions of the pixels hit are calculated and used for recording, in the corresponding pixel location, the number of background photons N_{bkd} as well as the number N_{e} of charge particles calculated within the relative depth by the GIL parameterization. N_{e} is converted in photoelectrons number N_{pe} as follows:

$$N_{\mathrm{pe}} = N_{\mathrm{e}} \cdot Y_{\mathrm{p}} \cdot A_{\mathrm{lens}} \cdot k_1 \cdot k_2 \cdot k_3 \cdot k_{\mathrm{m}} \cdot \Delta L/(4 \cdot \pi \cdot H^2)\,, \tag{14}$$

where Y_{p} is the photons yield, A_{lens} the pupil lens area, k_1 the transmission coefficient in ozone layer, k_2 the transmission coefficient in the atmosphere, k_3 the quantum efficiency of the MAPMT, k_{m} the transmission efficiency of the two lenses (including filter), and H the height of the orbit of the ISS.

The number of photoelectrons obtained from eq. (14) is then fluctuated according to the Poisson statistics and recalculated allowing for finite detector resolving time.

Background photoelectrons, N_{bkd}, are also generated in the same time unit using the following formula and then fluctuated around the mean value:

$$N_{\mathrm{bkd}} = \langle B_{\mathrm{bkg}} \rangle \cdot A_{\mathrm{lens}} \cdot k_3 \cdot k_{\mathrm{m}} \cdot \Delta\Omega \cdot t \tag{15}$$

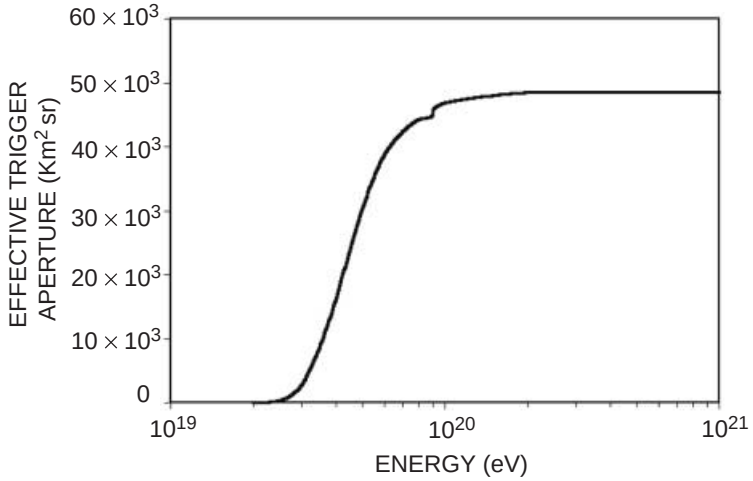

Fig. 21. – The effective trigger aperture for the EUSO configuration.

with $\langle B_{\rm bkd}\rangle$ representing the average photons nightglow background and $\Delta\Omega$ the pixel solid angle (the pixel size is assumed $= 0.8 \times 0.8$ km^2). Cloud coverage level has been introduced in the AWsim program as a parameter for allowing a more flexible and complete study of the experimental response to the possible different climate conditions.

In order to calculate the effective trigger aperture, angular resolution and rates, AWsim determines the minimum energy E which a shower of specified geometry must have in order to produce a sequence of signals in the focal surface detector pixels.

One of the criteria used in the reconstruction procedure requires the shower profile be available starting approximatively from 25% of maximum for the leading edge up to 25% of maximum for the trailing edge. In the presence of clouds, the reconstruction of the trailing edge has been limited to 60% of maximum, to take into account the smaller fraction of useful atmosphere. In this analysis showers landing inside the encircled ground area intercepted by the FOV of the EUSO telescope have been considered. Even within this limitation, the trigger aperture of EUSO for 10^{20} eV is about a factor 50 greater than the stereo trigger aperture of the HiRes experiment. A slightly greater value must be expected for the effective trigger aperture if the fiducial atmospheric volume intercepted by the FOV is considered instead.

Figure 21 shows the effective trigger aperture for the EUSO configuration; in simulating the events, the optics aperture ($\pm 30°$) and the quantum efficiency of the detector (20%) have been kept constant.

As the angular resolution is track length and energy dependent, an improvement of the angular resolution is expected for the more inclined tracks. The effect is evident in fig. 22 which shows the differences between input simulated zenith angle and reconstructed zenith angle $\Delta\theta$ in terms of standard deviations. Figure 23 quantifies the effect of 3-km and 5-km height cloud system on the basis of one-year EUSO collection of data. The tracks are partially hidden by clouds forbidding the reconstruction of those showers with zenith angle less of about 30° and 50°, respectively. The clouds coverage in fig. 23 is assumed to be 100% (non-realistic case).

The expected counting rates for the above-mentioned configurations have been obtained by folding the corresponding effective trigger aperture with the primary energy

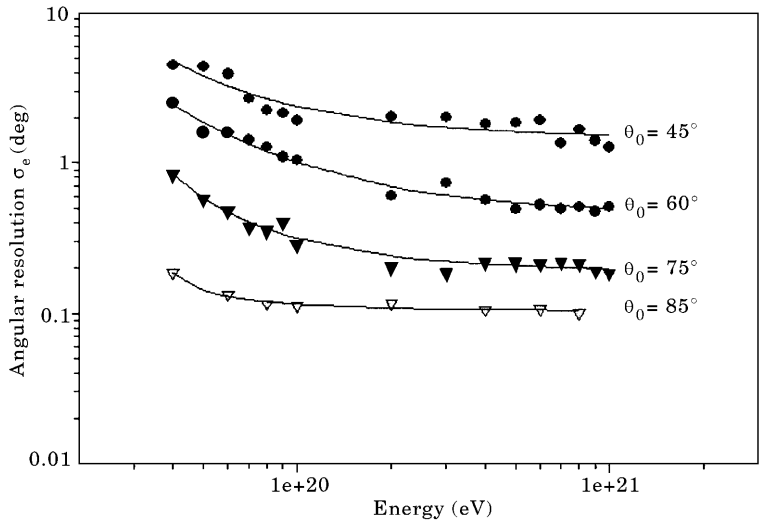

Fig. 22. – Angular resolution of simulated events. Significant improvement in the angular resolution is expected using the Čerenkov landmark signal.

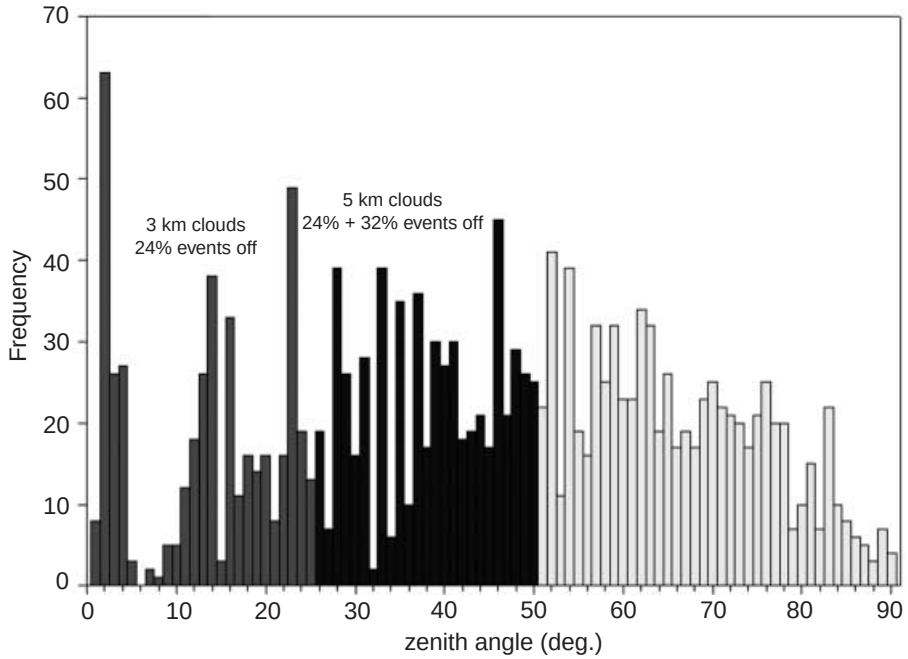

Fig. 23. – Percentage of the events dropped off in one EUSO observation year, using a no realistic 100% cloud coverage, for 3 km and 5 km height cloud distribution.

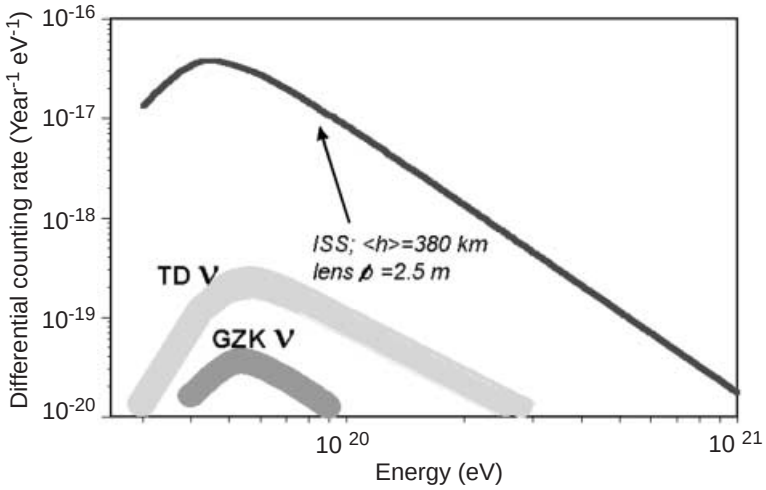

Fig. 24. – Differential counting rate of EECRs and neutrinos as expected for EUSO-ISS configuration. Topological Defects (TD) and GZK counting rates are shown.

spectrum given by AGASA [20] in the range 10^{19}–10^{20} eV and extrapolated to 10^{21} eV. A conservative duty cycle of 10% has been assumed. The counting rate takes into account only the events landing inside the FOV at the surface ground level. This choice has been preferred for accounting in the successive simulations the capability of the system in determining mass composition using the Čerenkov signal reflected by the impact surface (ground, sea or clouds).

Figures 24 and 25 show the expected counting rate curves as a function of the primary particle energy for the EUSO simulated configuration. Above 10^{20} eV, the expected counting rate is about 500 events/year (spectral index = 2.7).

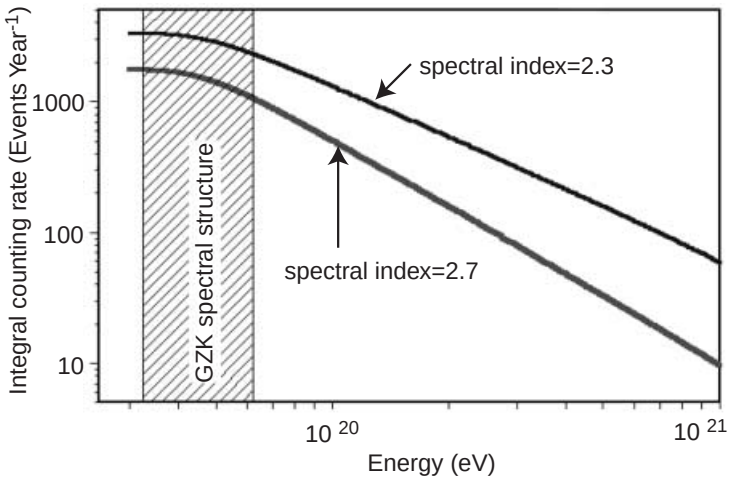

Fig. 25. – The expected counting rate as a function of the primary particle energy, for the EUSO simulated configuration, at two different spectral index values [20].

Quantitative assessment of fluorescence and background leads the detectable shower energy threshold at about 4×10^{19} eV. The expected energy resolution (energy depending) is $\sim$20%.

The long baseline provided by the extension up to ten thousand g/cm^2 of accessible atmospheric slant depth (corresponding to more than one hundred times the hadronic interaction length) and the good precision in localizing the characteristic $X_{\max}$ of the EAS development, make EUSO a powerful tool for the investigation of low interacting particles like neutrinos or other exhotic components. It should be noted also that EUSO exhibits the best angular resolution at very inclined zenith angles (fig. 22) for which a greater probability for neutrinos interaction (see fig. 3) is expected.

7. – Conclusions

EUSO is the first experiment devoted to the study of EECR and neutrinos from a space platform. And with the large exposure and full sky coverage, inherent to its geometry and mission profile, looks promising and challenging. The design of the telescope and the performance expected is the starting point for more ambitious future projects that will take advantage of the present pioneering work. The EUSO approach offers not only the possibility of covering large areas, but also the capability, using a compact monocular instrument, to detect the fluorescence light from the EASs with a much simpler and straightforward geometry compared to ground experiments. Future technological developments, especially in the detector devices and electronics associated, should improve the sensitivity and the overall efficiency in a such way to lower the energy threshold for detection of EAS below 10^{19} eV; the immediate effect will be the possibility of cross calibration with the ground-based experiments and the extension of the neutrino astronomy window at energies otherwise inaccessible.

* * *

I appreciate the support, help, encouragement and friendship of L. Scarsi, J. Linsley, M. C. Maccarone and B. Sacco, to whom I address my thanks.

REFERENCES

[1] Nagano M. and Watson A. A., *Rev. Mod. Phys.*, **72** (2000) 689.
[2] Linsley J., *Phys. Rev. Lett.*, **10** (1963) 146.
[3] Lawrence M. A., Reid R. J. O. and Watson A. A., *J. Phys. G*, **17** (1991) 733.
[4] Bird D. *et al.*, *Astrophys. J.*, **441** (1995) 144.
[5] Takeda M. *et al.*, *Phys. Rev. Lett.*, **81** (1998) 1163.
[6] Bierman P., *J. Phys. G*, **23** (1997) 1.
[7] Bhattacharjee P., *Observing giant cosmic ray air showers from* $> 10^{20}$ eV *particles from space*, in *AIP Conf. Proc.*, Vol. **433**, edited by J. F. Krizmanic, J. F. Ormes and R. E. Streitmatter (AIP) 1998, p. 168.
[8] Linsley J., *Call for Projects and Ideas in High Energy Astrophysic*, 1979.
[9] Kakimoto F. *et al.*, *Nucl. Instrum. Methods Phys. Res. A*, **372** (1996) 527.
[10] Baltrusaitis R. M. *et al.*, *Nucl. Instrum. Methods Phys. Res. A*, **240** (1985) 410.
[11] Sokolsky P., *AIP Conf. Proc.*, **433** (1998) 65.
[12] Auger Collaboration, Pierre Auger Project Design Report, 1997.
[13] Lebedinsky A.I. *et al.*, *Space Research*, 1966, p. 77 (in Russian).
[14] Catalano O. *et al.* to be published in *Nucl. Instrum. Methods Phys. Res. A* (2001).
[15] BG1 filters Rolyn Optics Catalogue, 1998.

[16] Hamamatsu Catalogue, 1999.
[17] Catalano O., *Observing ultrahigh energy cosmic rays from space and earth*, in *AIP Conf. Proc.*, Vol. **566**, edited by H. Salazar, L. Villaseñor and A. Zepeda (AIP) 2000, p. 145.
[18] Catalano O. *et al.*, AW Progress Report, IFCAI TechRep, March, 1999.
[19] Linsley J. *et al.*, private comunication, 1999.
[20] Yoshida S. *et al.*, *Astroparticle Phys.*, **3** (1995) 105.